Physical Modeling of Process Forces in Grinding

Praveen Sridhar ✉
Institute of Computational Physics in Engineering, Technische Universität Kaiserslautern, Germany

Daniel Mannherz
Institute of Computational Physics in Engineering, Technische Universität Kaiserslautern, Germany

Raphael Bilz
Institute of Computational Physics in Engineering, Technische Universität Kaiserslautern, Germany

Kristin M. de Payrebrune
Institute of Computational Physics in Engineering, Technische Universität Kaiserslautern, Germany

Mahesh R.G. Prasad
ICAMS, Ruhr-Universität Bochum, Germany

Juan Manuel Rodríguez Prieto
Mechanical Engineering Department, Universidad EAFIT, Medellín, Colombia

Abstract

This paper deals with material removal mechanisms in grinding by considering single grit-workpiece interactions. Individual investigations were performed both experimentally and using finite element simulations. Firstly, a comparison between the Johnson-Cooke material model and a Crystal Plasticity finite element method was performed with the help of micro-indentation experiments. Here the research question was answered if an anisotropic material model better describe the grinding process and process forces compared to an isotropic material model. Secondly, four discretization approaches were employed: pure Lagrangian (LAG), Arbitrary Lagrange Eulerian (ALE), Particle Finite Element Method (PFEM), and Smooth Particle Hydrodynamics (SPH), to simulate a micro-cutting operation of A2024 T351 aluminium. This study aims to compare the conventional approaches (LAG and ALE) to newer approaches (PFEM and SPH). The orthogonal cutting models were benchmarked against a micro-cutting experiment presented in literature, by comparing the obtained cutting and passive forces. The study was then extended to negative rake angles to study the effect on the discretization approaches for grinding. Thirdly, scratch experiments were investigated for a brittle material sodalime glass and A2024 T351 aluminium. Effects of the linear speed of the device, depth of cut, and conical tool angle were analyzed and tendencies are built. Finally, a realistic simulation of the manufacturing process of a grinding wheel was developed, starting with the raw material, compression, sintering, and dressing until the final grinding surface. As a result of the simulations, virtual grinding wheel topographies can be visualized and analyzed with regard to the output variables from grinding wheels such as bonding strength and static grain count. The individual research studies help in understanding the material removal mechanisms in a single grit scratch process as well as in the understanding of the overall grinding wheel topography. This in turn helps in the developing an overall physical force model for scratching/grinding to predict mechanical output parameters and hence reduce the need for experimentation.

2012 ACM Subject Classification Computing methodologies → Modeling and simulation

Keywords and phrases grinding, single grit approach, finite element method, smooth particle hydrodynamics, particle finite element method, scratch experiments, virtual grinding wheel model

Digital Object Identifier 10.4230/OASIcs.iPMVM.2020.16

Funding This research work was funded by the Deutsche Forschungsgemeinschaft (DFG, German Research Foundation) Project ID– 252408385 – IRTG 2057 and Project-ID 172116086 – SFB 926.

Acknowledgements The authors would like to thank Matthias W. Klein, Marek Smaga and Tilmann Beck from the Institute of Material Sciences and Engineering at Technical Universität Kaiserslautern for their collaboration and for providing us with the experimental data used in section 2.

2nd International Conference of the DFG International Research Training Group 2057 – Physical Modeling for Virtual Manufacturing (iPMVM 2020).
Editors: Christoph Garth, Jan C. Aurich, Barbara Linke, Ralf Müller, Bahram Ravani, Gunther Weber, and Benjamin Kirsch; Article No. 16; pp. 16:1–16:20

OpenAccess Series in Informatics
OASICS Schloss Dagstuhl – Leibniz-Zentrum für Informatik, Dagstuhl Publishing, Germany

1 Grinding and Single Grit Scratch Approach

Grinding is a form of material removal applied to many metals and ceramics, especially hard-to-machine materials, to obtain smooth surfaces on products within a desired tight tolerance. Grinding mechanics and material removal mechanisms are complex and the processes are still not fully understood. In the manufacturing industry, almost 65 % of machining companies use the grinding process [5] and a significant portion of production cost is due to grinding or related abrasive processes. However, some experimental observations are difficult to explain theoretically due to the complex nature of the process mechanisms. Also, the determination of some of the mechanical characteristics, e.g., stresses, strains, and temperature distribution across the machined surface are difficult to obtain experimentally and the grinding process analysis using experimental tests could be both costly, owing to the high price of grinding tools, and not generally valid as the results obtained might be valid only for a certain machining condition [17]. Thus, the prediction of mechanical parameters such as forces, strains, stresses, and surface deformations that occur during grinding using computer technology is a valuable tool of getting additional insight into the final quality of machined surface and to reduce costly experiments.
The grinding process is a material removal process using a grinding wheel, which is made up of a large number of randomly oriented abrasive particles. The grinding operation is performed at relatively high speed and the undeformed chip thickness is relatively small particularly in fine grinding operations compared to other machining processes. To measure the grinding performance, the grinding system behavior must be evaluated properly. The grinding system behavior is mainly assessed by considering abrasive geometry, kinematics, mechanics, and energy and material properties[17]. The Overall grinding performance including the finish surface quality is directly related to the performance of the grinding wheel used during the grinding operation. The performance of a precision grinding wheel is usually determined by using the parameters such as grinding force, machining vibration, the temperature in the cutting zone, and workpiece surface roughness.

Material removal mechanisms for grinding can be categorized into two groups: (i) removal mechanisms during grinding wheel-workpiece interaction and here investigations will be at the macroscale, and (ii) removal mechanisms considering single grit-workpiece interaction and investigations will be at the microscale.
The following individual studies were performed under these two groups:

- Parametristaion of a material model employed in the finite elemenet (FE) model is important in the prediction of the process variables in a single grit scratch process. Here a research study is performed to compare an isotropic Johnson-Cooke model with an anisotropic crystal plasticity FEM model with help of micro-indentation tests, to understand the effect of the choice of a material model (ref section 2).
- A FE material removal model is developed to understand the cutting mechanism taking place during a single grit scratch. The model studies in detail the effect of change in the tool geometry (rake angle) on the process forces. Furthermore, the individual models are discretized using different available discretizational approaches, to understand its advantages and drawbacks, as described in section 3.
- Experimental investigations of single grit scratching is performed using shaped tool geometries with high rake angles between -45° to -75° for a brittle material (glass) and a ductile material (aluminium), ref section 4.
- A realistic simulation of the manufacturing process of a grinding wheel, starting with the raw material mixing, compression, sintering, and dressing until the final generation of a

grinding surface is done in section.5. This research studies the effect of different levels of compression, i.e. the percentage of compression and compression force on grinding wheel measurements such as static grain count and bonding forces.

2 Material Modelling and Parametrisation

In a finite element simulation, material modeling and its parametrization is an innate aspect in predicting the material behavior when subjected to different loading conditions. Specifically, grinding is a surface finishing process involving the interaction of multiple abrasive grains onto a workpiece. Interestingly, in this manufacturing process, the crystal grain size of the workpiece material is in the same range as the removal depth. Hence, a fundamental research question arises: *does an anisotropic material model better describe the grinding process and predict the process forces compared to an isotropic material model?* As grinding is a complex material removal process, initially a simple micro-indentation model is chosen to validate and compare two plasticity models. To describe the anisotropic polycrystalline model, the crystal plasticity finite element method (CPFEM) is employed, and to describe the isotropic model, the Johnson-Cooke plasticity model is chosen. In this study, micro indentation experiments were performed on twinning induced plasticity (TWIP) steel and the respective force-displacement curves were obtained. These curves were subsequently used to validate the chosen plasticity models.

2.1 Experimental Investigations

The experimental investigations of the high manganese HSD600 TWIP steel were performed by Klein, et al. [11]. Firstly, the microstructure of HSD600 showing the grain size distribution and grain orientation mapping is obtained by electron backscatter diffraction (EBSD). The average equivalent grain size was found to be 8.6 μm. The data obtained from the microstructural analysis were used as inputs in the development of the CPFEM model. Secondly, cyclic micro-indentation tests were performed on HSD600 using a Vickers indenter. The specimens were subjected to a maximum load of 1 N for a loading cycle of 6 seconds and the applied load was gradually reduced during the unloading cycle of the following 6 seconds. The load-displacement curves obtained from the micro-indentation tests (ref Fig.1) were used as the basis to validate and compare the results from the FEM simulations.

2.2 Simulation Framework

For the isotropic material model, the Johnson-Cooke material model (JC-model) was employed. This computational model for flow stresses includes the effects of strain hardening, strain rate hardening, and thermal softening. The von Mises flow stress σ, is expressed as the product of the three uncoupled terms,

$$\sigma = [A + B(\varepsilon)^n] \cdot \left[1 + C \ln\left(\frac{\dot{\varepsilon}}{\dot{\varepsilon_0}}\right)\right] \cdot \left[1 - \left(\frac{T - T_{room}}{T_{melt} - T_{room}}\right)^m\right]. \tag{1}$$

In here, A is the quasi-static yield stress, B is the modulus of strain hardening, n is the work hardening exponent, C is the strain rate sensitivity and m defines the temperature sensitivity. The material parameters were initially obtained from [11, 26], although parameter optimizations were performed to obtain a better fit to the experimental results. The simulations of the micro-indentation were performed using the commercial FEM program Abaqus/Standard (version 2019) with the optimized JC-model parameters listed in Table 1.

Table 1 Optimized isotropic Johnson-Cook material parameters.

A [MPa]	B [MPa]	C	n	m
619.96	1642.68	0.098	0.29	1.402

For the anisotropic material model, to predict the response in a polycrystalline material, the whole material is approximated by smaller, periodically repeating material elements, commonly referred to as representative volume element (RVE). The RVE was generated based on the average grain size and texture obtained from the EBSD analyses. The crystal plasticity (CP) model employed to reproduce the plastic deformation in the RVE is implemented based on the model described in [22]. The flow rule that expresses the accumulative shear rate at each slip system α is given by

$$\dot{\gamma}_\alpha = \dot{\gamma}_0 \left| \frac{\tau^\alpha}{\hat{\tau}^\alpha} \right|^{p_1} \operatorname{sgn}(\tau^\alpha), \tag{2}$$

where $\dot{\gamma}_0$ is the reference shear rate, p_1 is the inverse of the strain rate sensitivity, τ^α is the resolved shear stress and $\hat{\tau}^\alpha$ is the slip resistance, which describes the hardening behavior of the material. Simulations were performed using Abaqus/Standard through a UMAT (user defined material subroutine) with the following optimized CP parameters in Table 2.

Table 2 Optimized CP parameters for HSD600 TWIP steel used in the CPFEM simulations. The elastic constants were obtained from [18].

C_{11}[GPa]	C_{12}[GPa]	C_{14}[GPa]	p_1	p_2	$\dot{\gamma}_0$ $[s^{-1}]$	$\hat{\tau}_0^\alpha$	$\hat{\tau}_f$[MPa]	h_0[MPa]
174,000	85,000	99,000	13	2.25	0.001	200	900	1600

2.3 Results

Fig.1. shows the force-displacement curves from the micro-indentation experiment of HSD 600 TWIP steel, in comparison to the simulation results of the isotropic JC-model and the anisotropic CPFEM model. On first glance, both material models show a good agreement with the experimental results. Both models closely predict the maximum displacement of 3.6 μm at a maximum load of 1 N. On looking closely at the material response during the loading cycle, both models show a similar response during the elastic domain. As the curves progress towards the plastic domain, there is a divergence of the simulation results compared to the experimental result. The fitting to the experimental data is a little better for the CPFEM model when compared to the JC-model, because the CPFEM model incorporates explicitly the polycrystalline microstructure in contrast to the isotropic JC-model, which does not.

However, the isotropic JC-model is good enough to predict the material behavior of a ductile material and could further be optimized with the help of the CPFEM model by parameter linking. In further studies, EBSD analysis and micro-indentation are planned to be performed on aluminium A2024 T351 and the parameterized isotropic JC-model is used in the scratch simulation to be validate by experiments.

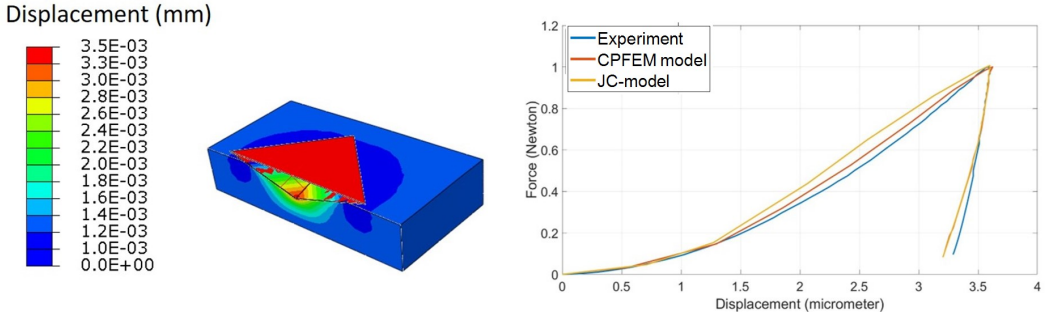

Figure 1 Comparison of force-displacement curves from micro-indentation of HSD 600 TWIP steel between anisotropic CPFEM and isotropic JC-model.

3 Numerical Simulations and 2D Cutting Model

Simulating dynamic machining processes by simplifying the real system is quite commonly used to predict machine behavior and understand the influence of machining parameters on both, tool and workpiece. With increasing computational power it is easier to solve complex problems such as abrasive grit-workpiece interactions [17]. A well-designed simulation model of the grinding wheel could largely reduce the cost of experimentation and successfully determine the grinding process behavior based on the surface finish of the machined part, workpiece characteristics, material removal mechanisms, and tool wear. In addition, simulations are able to provide some extra information like stresses, strains, strain rates, and temperature gradients, which are otherwise extremely difficult to determine by experimental investigations.[17] As grinding is one of the most complex machining processes, there is no universal model to comprehensively predict the machining behavior in terms of the grinding forces, material removal, and surface finish. Hence different numerical approaches are studied in terms of their advantages and drawbacks in modeling grit workpiece interactions.

3.1 Discretization Approaches

In continuum mechanics, the motion of a material point can be described using three algorithms namely the Eulerian, Lagrangian, and Arbitrary Lagrangian-Eulerian methods. In addition, meshless methods like smooth particle hydrodynamics and particle finite element can be employed to describe the material motion.
As part of the comparative study, the two mesh-based methods Lagrangian (LAG) and Arbitrary Lagrangian-Eulerian (ALE) approach, and two particle-based methods Smooth Particle Hydrodynamics (SPH) and Particle Finite Element Method (PFEM) are used to perform cutting simulations of A2024 T351 aluminium. As an outcome of the study, the solution accuracy of the forces, stresses, and temperatures inside the workpiece is compared between the mesh-based methods and particle-based methods for different cutting conditions.

3.1.1 Mesh Based Methods

The Lagrangian (LAG) approach is most often used in solid mechanics problems, where the displacement vector tracks the individual material points. However, its inability to follow large deformation can lead to simulation failures. Possible solutions, as implemented by [15], are either element deletion, which leads to a reduction of mass, or adaptive remeshing. However, in adaptive remeshing, the diffusion of internal variables while mapping from mesh to mesh may invalidate the numerical results of the simulation.

In the Arbitrary Lagrange Eulerian (ALE) approach, the mesh is neither constrained to a fixed space (Eulerian approach) nor does it move along with material points (Lagrangian approach). The ALE approach helps to maintain the mesh topology and avoid iterative meshing. A smoothening algorithm is applied to relocate the nodal positions of the mesh to avoid problems of mesh distortion and hour glassing, as in a similar implementation of [16]. Although the ALE method is computationally effective, the accuracy is still limited to the underlying mesh and the choice of the smoothening algorithm. For the cutting simulations presented in this work, both discretization approaches are used. The workpiece and tool were both modeled in 2D and discretized with temperature coupled quadrilateral continuum elements. The thickness of both bodies was set to 1 mm, similar to the feed width of cut a_p of experiments conducted in [1].

3.1.2 Particle Based Methods

The Smooth Particle Hydrodynamics (SPH) method differs from the above-mentioned techniques since it is categorized as a meshless method. The material domain is discretized by spheres, which can have a strong connection in the case of solids or a weak connection in the case of liquids. Due to the weak bonding of the adjacent particles, a failure criterion is not necessary, since the material separation occurs due to the loss of cohesion between the particles. In the SPH simulation, the cutting tool is modeled as a rigid body, which means that the heat transfer between tool and workpiece cannot be simulated. However, material parameters are provided for the contact analysis.
The Particle Finite Element Method (PFEM) was first introduced by [7] for fluid-structure interaction problems. It combines the benefits of continuum based methods and discrete modeling techniques, therefore it is well suited for problems with large deformations and large configuration changes. In contrast to classical finite element approximations, in PFEM the deformation of the body is calculated by the underlying set of particles. At the end of each time step, a mesh is built upon the particles with their centerpoints as nodes. For this reason, a fast and robust algorithm is essential to build a new mesh. In this work, the *Delaunay Tessellation* method is chosen to connect all particles at the current time step position and creating the new mesh. The particles of the PFEM simulation are spheres and the generated mesh is an unstructured mesh with 2D triangular elements. The diameter of the particles and the thickness of the mesh elements were again set to a feed width of cut $a_p = 1$ mm. The resulting mesh not only works as support where the differential equations are integrated, but is also used to identify contacts and to track free surfaces. The track of the surface is accomplished with the help of a technique called alpha-shape as implemented by [7]. An application of PFEM to the numerical modeling of metal cutting processes can be found in [20].

3.2 Material Model and Damage Model

In metal cutting large strains, large strain rates and high temperatures occur in the primary and secondary shear zones. A material model that describes the material behavior under these conditions is the Johnson-Cook material model, with its mathematical description provided in the previous chapter (Eq.1) [9].

In order to consider material damage, the Johnson-Cook damage model [9] is used in conjunction with the Johnson-Cook material model. Eq. 3 provides the expression for the failure plastic strain $\bar{\varepsilon}$,

$$\bar{\varepsilon} = \left(D_1 + D_2 \exp\left(D_3 \frac{\sigma}{\bar{\sigma}}\right)\right) \cdot \left(1 + D_4 \ln \frac{\dot{\bar{\varepsilon}}}{\dot{\varepsilon}_0}\right) \cdot \left[1 - D_5 \left(\frac{T - T_{room}}{T_{melt} - T_{room}}\right)^m\right]. \tag{3}$$

The fracture energy model proposed by Hillerborg [6, 3] is included in the model to determine the damage evolution. After damage initiation, the damage variable D varies by the ratio of the yield plastic deformation to the failure of plastic deformation. After damage has been initiated for $D > 0$, the new values for yield strength σ and Young's modulus $\tilde{E}$ can be calculated using $\sigma = (1 - D)\bar{\sigma}$ and $\tilde{E} = (1 - D)E$. Hence, the Johnson-Cook material model and the Johnson-Cook damage model describe linear elasticity, strain hardening and thermal softening, damage initiation, damage evolution, and eventually fracture. The used material and damage parameters are listed in Table 3.

Table 3 Johnson-Cook material parameters and damage coefficients for A2024 T351 aluminium.

A [MPa]	B [MPa]	C	n	m	$D1$	$D2$	$D3$	$D4$	$D5$
598	768	0.0137	0.2092	0.807	0.01	0.13	3.1	0	0

3.3 Contact Model and Heat Generation

The contact between tool and workpiece is described by a penalty contact algorithm. The tool is defined as master surface and the workpiece is defined as slave surface. It is to be noted that the mesh of the workpiece is fine enough to avoid penetration of the tool during contact. The Coulomb friction law is used in the contact model. It relates the frictional stress τ_f to the normal stress σ_n times a constant coefficient of friction μ, where $\mu = 0.23$ is chosen based on the previous works of [1, 21].

Since the temperature has a large impact on the accuracy of the machining simulations, a thermo-mechanical coupled problem is solved. The total heat flux $\dot{q}$ is calculated as the sum of the heat flux due to plastic strain with $\dot{q}_p = \eta\bar{\sigma}\dot{\varepsilon}^p$, and the heat flux due to friction in the tool-chip interface with $\dot{q}_f = \tau_f v_r A$. In here is η the inelastic heat fraction with η =0.9, $\bar{\sigma}$ the effective stress without damage, $\dot{\varepsilon}^p$ the plastic strain rate, τ_f the frictional stress, v_r the relative velocity and A the contact area between tool and chip. The temperature rise in the chip can be approximated as adiabatic heating according to [17] and the thermal energy generated is distributed evenly over the tool and the workpiece.

3.4 2D Micro Model of Single Scratches

This section provides information on the simulation framework of the 2D micro-cutting model, the performed benchmark simulation and sensitivity analysis. The model parameters of an orthogonal cutting process were chosen according to [25]. In an experiment by [25], a straight turning operation was performed on A2024 T351 aluminium (Young's modulus= 73 GPa, Poisson ratio= 0.3 and density=7800 kg/m^3) by a high speed steel (HSS) insert (Young's Modulus= 680 GPa, Poisson ratio= 0.33 and density= 7830 kg/m^3) with the orthogonal rake angle $\gamma = 20°$ and a clearance angle $\alpha = 5°$. The feed per revolution was set to $f = 50$ μm typically seen in grinding processes, with a constant $a_p = 1$ mm along the thickness of the workpiece and a cutting speed $v_c =$ 180 m/min. The simulation results are validated according to this experiment. In the simulation framework the element spacing d_e for the LAG/ALE models and particle spacing d_p for the SPH/PFEM models where $d_e = d_p = 0.003$ mm.

3.4.1 Benchmark Simulation

To validate the different discretization approaches LAG, ALE, SPH, and PFEM with real data, a benchmark analysis was conducted for the dry-turning operation of A2024 T351 aluminium with rake angle $\gamma = 20°$ and compared with the results from literature [25]. Fig.2 illustrates the calculated process forces and the measured forces from [25] of the reference cutting process with $\gamma = 20°$. The average measured cutting force in x-direction is 50 N in the stationary state of the experiment. The discretizations LAG, ALE and SPH predict the cutting force in good agreement with the experiment, with a minor error of 1 %. Only the PFEM approach underpredicts the cutting force with an error of 8 %. However, comparing the passive force, all the discretization approaches underpredict is with an error of 40 %. The reason for lower prediction of passive forces, in the mesh-based methods could be the settings of the built-in element deletion during material separation in the sacrificial layer. As elements are deleted that have been deformed beyond a threshold value or exceed a predefined stress value, the contact between tool and workpiece reduces and the passive force decreases. In contrast, the meshless models have a weighting function that determines the force required to release the cohesive bonds. The progression of the cohesive forces used in this work decreases in a bell-shaped manner within the area of influence, which could cause an early separation of the particles.

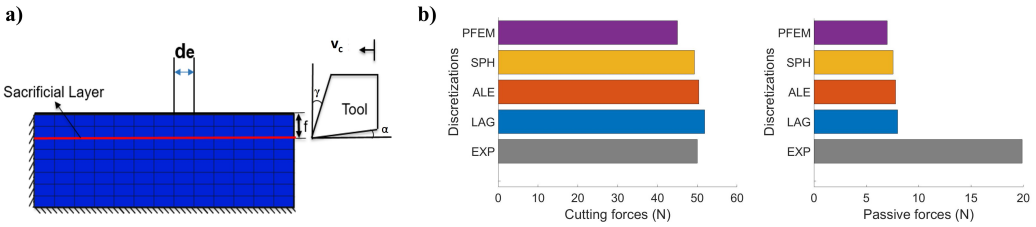

Figure 2 a) Simulation framework of the benchmark simulation and b) Comparison of the cutting/passive forces of the discretizational approaches with the experimental results from [25].

3.4.2 Sensitivity Analysis

This section presents the results of the sensitivity study when increasing the tool rake angles, towards high values between $\gamma = 0°$ to $\gamma = -45°$, typically observed in the cutting mechanisms in grinding. Comparing the process forces (cutting forces/passive forces) for the six rake angles, an increase is observed in Fig.3 with an increase in the negative rake angle γ. As the contact length at the tool-workpiece interface increases for a higher negative rake angle, this induces higher compressive stresses and plastic strains on the workpiece, which explains the increase in the process forces. The increase in the process forces is also confirmed by investigations done by [12].

4 Experimental Investigations

The grinding process involves extremely complex material removal mechanisms because of the numerous irregularly shaped and sized abrasive grits bonded onto the grinding wheel. A grinding process can be modeled as a cumulative process of the result of several single grit actions over the workpiece, thus the single grit interaction with the workpiece is of essential importance. With an understanding of individual grit-workpiece interaction mechanisms, the material removal phenomena can be extrapolated to the entire grinding wheel-workpiece interaction.

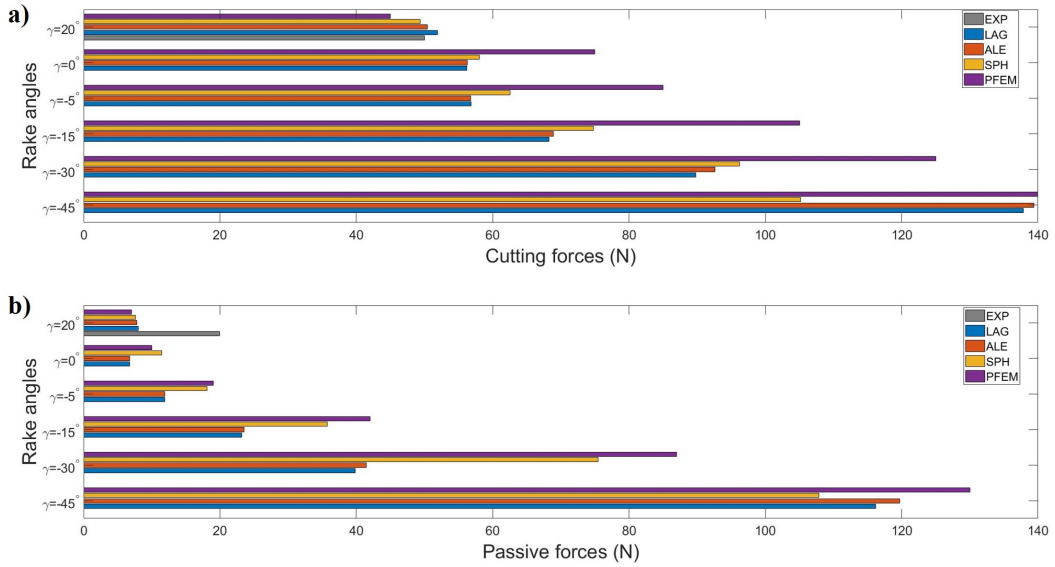

Figure 3 Comparison of the discretization approaches LAG, ALE, SPH and PFEM based on a) cutting forces and b) passive forces for the tool rake angles $\gamma = 20°$ to $\gamma = -45°$.

4.1 Experimental Setup

In this investigation, single grit grinding tests were performed on two different workpiece materials, a ductile material A2017-T4 aluminium and a brittle material soda lime glass. Scratch grooves were cut by single grit actions performed at different speeds and with gradually increasing depth of cut. A force sensor was used during the single grit grinding process to record the force exerted during scratching. The experimental setup with an exemplary force measurement is shown in Fig.4.

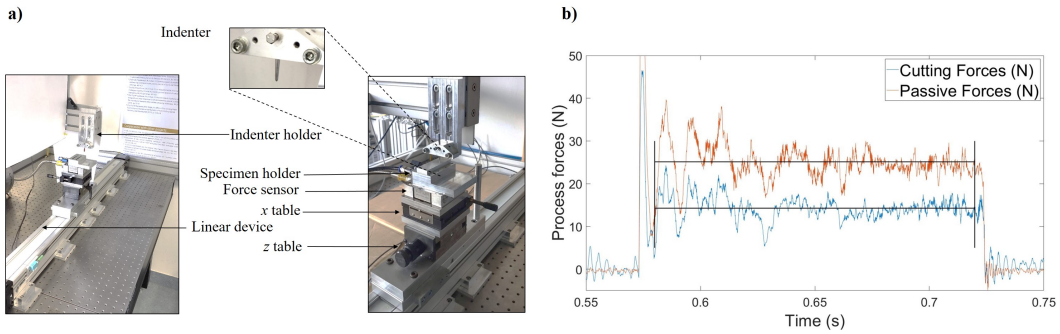

Figure 4 *a*) View of single grit scratch test setup and *b*) forces recorded with LabView software (v_c=100 mm/s on A2017 T4 workpiece).

The experimental setup consists of a linear motion device of stroke length of 850 mm. The linear axis is mounted with a z-table on the linear device, to set the depth of cut. A screw with a resolution of 1 μm drives the vertical movement. The x-table enables the motion along the horizontal direction, used to demarcate one scratch from the other. A Kistler 3-axis force sensor (Type: 9119AA1) was mounted under the workpiece to measure the forces during single grit scratching. The aluminium and glass samples are mounted on the specimen

holder with the help of vacuum, an indenter holder is fixed along a vertical column. The force measurement acquisition was performed using the LabView 2018 software package. The sampling rate was 10,000 samples/sec. The Fig.4b shows a sample measurement performed for a scratch experiment with A2017 T4 (depth of cut a_p=50 μm and linear speed v_c= 100 mm/sec). The single grain scratch tests were performed with conical indenter geometries, with cone angles 90° and 120°, as shown in Fig.5.

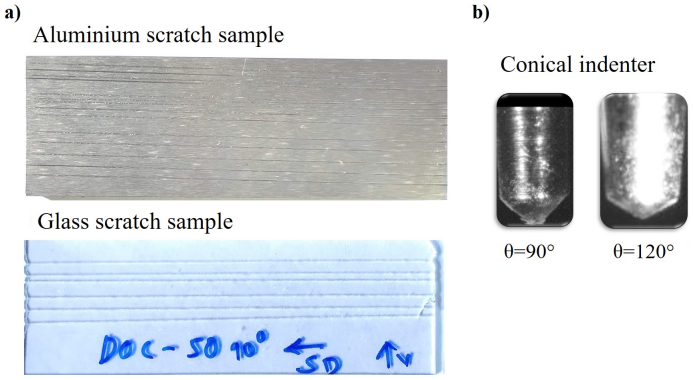

Figure 5 *a*) Single grit scratches (v_c =50 mm/s to 300 mm/s for a_p = 50 μm) on A2017 T4 and soda lime glass samples and *b*) conical indenter geometries $\theta = 90°$ and 120°.

4.2 Scratch Experiments

The scratch experiments were performed on soda lime glass samples of dimensions 75 mm × 25 mm × 1 mm. Fig.6 show process forces measured during scratch experiments performed on soda lime glass for the depth of cuts 50 μm, 70 μm and 80 μm. The scratch experiments/measurements were performed three times for all depth of cuts at various linear speeds. The statistical average of the process forces obtained, is used for the analysis. In the 3D bar plots the x-axis shows the speed of the linear device, the y-axis shows the rake angle of the indenter tool and the z-axis shows the cutting forces and passive forces in N.
According to Fig.6a, it can be seen that the cutting forces reduces with increase in speed of the linear device, for all the three depth of cuts a_p=50 μm, 70 μm and 80 μm. While comparing the cutting forces between the two conical angles (90° and 120°) for the lowest depth of cut a_p=50 μm, it is observed that the cutting forces is higher for the conical angle of 120° than for 90°. This is because the 90° conical angle appears to have the sharper tool tip, which reduces the cutting forces. However this tendency seems to invert for the higher depth of cuts a_p=70 μm and 80 μm . With the higher depth of cuts, it is observed that the 90° conical angle has undergone higher wear in comparison to the 120° conical angle. As a results the cutting action is performed by blunter cutting edges, leading to higher cutting forces measured for the indenter with the 90° conical angle.

According to Fig.6b, it can be seen that, the passive forces more or less remains constant with increase in speed of the linear device, for the depth of cuts a_p=50 μm and 70 μm. Although for a higher depth of cut of a_p=80 μm, there is a reduction in the passive forces with increase in speed of the linear device. This is observed due to formation of local damage in the scratched glass specimen. The cracks developed and propagated between the individual scratches can explain this change in the tendency. From the indenter geometry pictures in Fig.5b, we can observe that the 90° tool has higher roundness compared to the 120° tool at the tool flank. This also exerts a higher contact area on the workpiece while scratching.

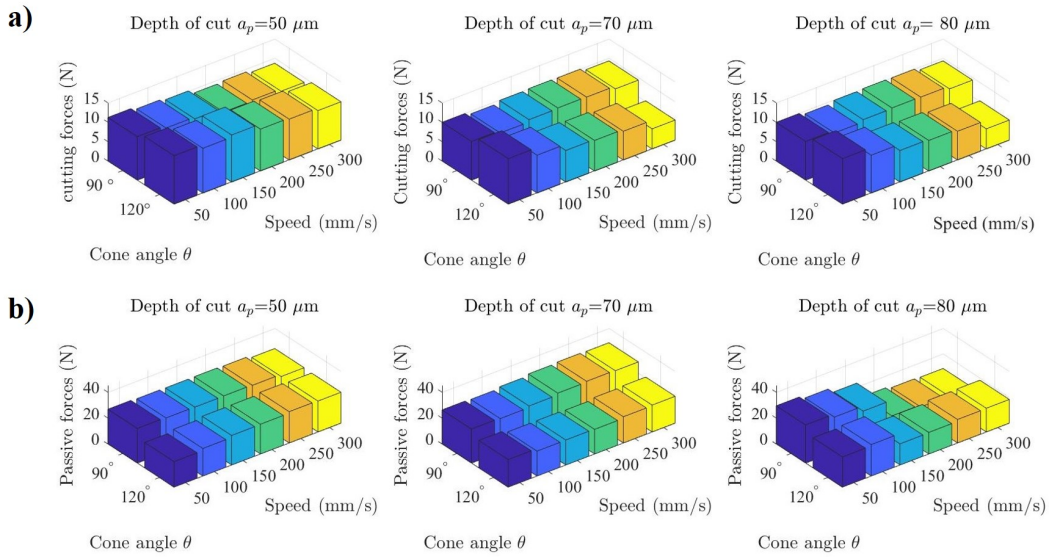

Figure 6 3D bar plots showing the measured *a*) cutting forces and *b*) passive forces, for the linear speeds v_c=50 mm/s-300 mm/s and depth of cuts a_p=50 μm, 70 μm and 80 μm.

Taking this into aspect, while comparing the passive forces between the two conical angles (90° and 120°) for depths of cut a_p=50 μm and 70 μm, the passive forces for the 120° conical angle is lower than for the 90° conical angle. Although for a higher depth of cut a_p=80 μm and for higher speeds v_c= 200-300 mm/sec the passive forces is observed to be higher for the 120° conical indenter. As the with the higher depth of cuts, it is observed that the 90° conical angle has undergone higher wear in comparison to the 120° conical angle, thereby the cutting forces increases and the passive forces decreases.
Beside the analysis of the conical angle and linear speed on the process forces of brittle soda lime glass, the effect of the speed on the process forces is additionally evaluated on aluminium 2017 T4 samples. The scratch experiments were performed on the aluminium 2017 T4 samples of dimensions 75 mm × 25 mm × 5 mm. Fig.7 shows process forces measured during scratch experiments for various speeds of the linear device v_c= 50-1000 mm/sec. According to Fig.7 and the experiments performed by [17], it can be observed that the cutting and the passive forces reduce with an increase in the speed of the linear device.

5 Virtual Grinding Wheel Modeling

Grinding wheels are one of the most important tools in the manufacturing process of high precision and high quality surfaces. This study aims to provide a realistic simulation of the manufacturing process of a grinding wheel, starting with the raw material, compression, sintering and dressing until the final grinding surface. Furthermore, it researches the effect of different levels of compression and grit sizes (F24 to F60) on the surface topography. The analysis of static grain count and bonding forces were made on the generated grinding wheel topographies. The quality of grinding wheel topographies were assessed and practical consequences were drawn for improving the manufacturing process.

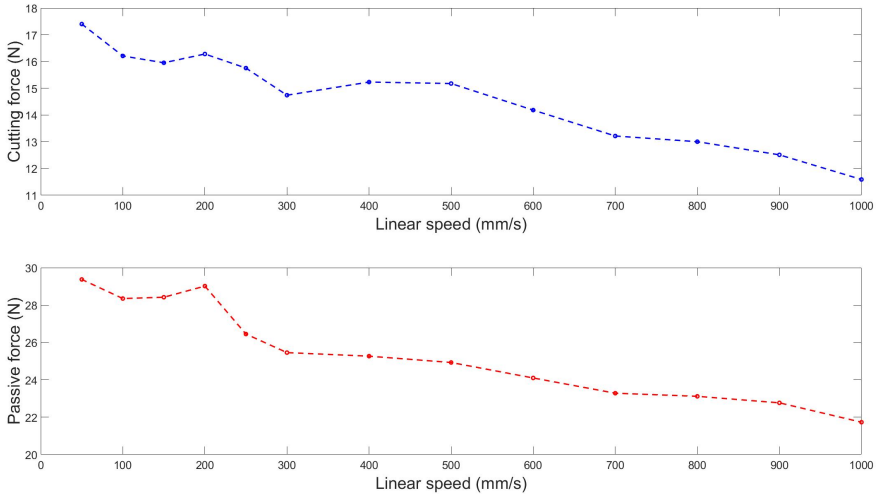

Figure 7 Process force measurements with an 120° conical angle indenter for the linear speeds v_c =50 mm/s-300 mm/s and depth of cuts a_p=50 μm on A2017 T4 specimens.

5.1 Simulation Framework

To create a realistic model, but also one that is feasible and computable without high amounts of computation power, only a cut-out of a real grinding wheel is simulated. The cut-out is displayed in Fig.8 and contains a surface-side, which is equal to the grinding surface of the grinding wheel.

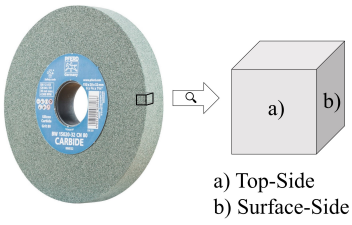

Figure 8 Grinding wheel cut-out used for simulation.

The first step in the manufacturing of a grinding wheel is weighting the raw material, i.e. the amount of bond material and abrasive particles. Afterwards, the materials are being mixed. During this process, pores are being created and their distribution is defined by the natural packing between the two components [2]. In the third step, the mixture is put into a steel form of the desired grinding wheel shape and compressed by a hydraulic press. The first three steps of the simulation were conducted with the discrete element (DEM) simulation software LIGGGHTS. After this, particles are being fired (sintered) and dressed resulting in the final grinding wheel surface. Those two steps were simulated with MATLAB, using the particle output from LIGGGHTS.

5.1.1 Particle Packing and Compression

The material mixing in the simulation was done by creating particles where the bonding material is already surrounding the grain, in comparison to the real manufacturing, where this step is happening while mixing the materials. The creation of particles in LIGGGHTS was done by a stepwise creation of new particles. The particles were randomly distributed in a certain area above the form, representing the natural distribution of the materials. The particles start falling immediately after their creation and the whole system is settled down after the creation of particles is stopped. Additional particles outside the desired shape were removed. The particles created are composite of the abrasive grain with radius R_{gi} and the correspondent amount of bond material, resulting in the total particle diameter R_{pi}, as displayed in Fig.9a .The total particle diameter R_{pi} is dependent on the distribution of bond material f_b and abrasive grain f_b, as well as the grain diameter R_{gi} [14]

$$R_{pi} = R_{gi} \cdot \left(1 + \frac{f_b}{f_g}\right)^{(1/3)} . \tag{4}$$

The applied hydraulic pressure is usually between 100-5000 PSI ($0.69 - 34.5$ N/mm^2) and is applied for about 10-30 seconds [14, 8]. The simulation in this study was volume controlled, i.e. the top cylinder is moved by a certain distance per unit time towards the bottom, which is a good representation of the real manufacturing process [10]. A visual example of the compression process is displayed in Fig.9b. The maximum feasible compression is defined as the compression reached when more than 0.5 % of the particles had a radius less than their initial grain radius R_{gi}. Thus, the simulation represents the difference in material properties of the outer bond material and inner abrasive grain, as the abrasive grain is by far less compressible. Abrasive grains, e.g. silicon carbide, have a Young's modulus of 400 GPa [23], whereas the bond material, e.g. epoxy resin, only has a Young's modulus of 6.2GPa [19].

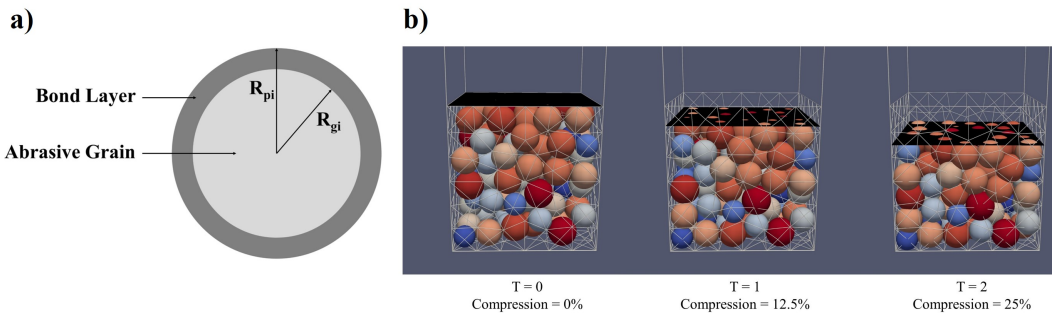

Figure 9 a) Representation of particle and bond material and b) particle packing and compression simulation.

5.1.2 Firing

The firing (sintering) of the specimen is simulated using MATLAB and uses the exported particle data from LIGGGHTS, containing the position and radius of every particle, as well as the contact surface area of the connection. The first step in the firing algorithm is the calculation of the new neck radius a, as displayed in Fig.10. The characteristic time for the grain-boundary diffusion t_g is used as a material property [27] and the sintering (firing) time for the grain-boundary diffusion [27] needs to be set. With the use of the old (initial) neck radius a_0, the formula for the new neck radius calculation is [14, 27]

$$a = a_0 \cdot \left(\frac{192t}{t_g} \right)^{(1/6)} \cdot \tag{5}$$

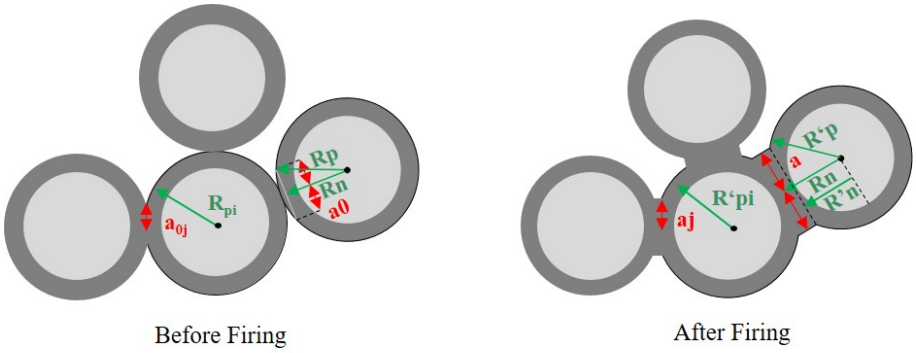

Figure 10 Change in the topology a) before and b) after the firing process with displayed characteristic geometrical values.

In Fig.10. the formation of multiple particles before and after firing is displayed. Each particle i in the set of n particles has a radius R_{pi} before firing and a radius R'_{pi} after firing. Every connection of a particle (bond j in the set of m connections has a neck radius a_{0j} before firing and neck radius a_j after firing). The calculation of the particle radius R_{ni} (see Fig.11), which connects the particle centre with the respective middle point of the neck, is calculated using Pythagoras $R_n = \sqrt{(R_p^2 - {a_0}^2)}$. The calculation of the new particle radius is based on mass conservation.

$$\left(\frac{4}{3} \cdot \pi \cdot R_{pi} \right)^3 = \left(\frac{4}{3} \cdot \pi \cdot R'_{pi} \right)^3 + \sum_{i=1}^{n} \sum_{j=1}^{m} ({a_i}^2 \pi \cdot (R_{ni} - {R'}_{ni}) - \frac{\pi}{3} {h_j}^2 \cdot (3{R'}_{pi} - h_j)) \tag{6}$$

5.1.3 Dressing

The dressing of the grinding wheel is usually conducted by a single-grit diamond [13] to reduce thickness, to correct balance or parallelism, or to create special contours (e.g. sharp edges) [14]. When the dresser hits a particle, there are three different possible situations. The first possibility is that the dresser hits the particle at its full surface, resulting in a removal of the grit, independent from dressing force or bonding force. The second option is that the dresser partly hits the particle, but the dresser force is higher than the bonding force of the particle, resulting also in a removal of the grain. The third option is that the dresser partly hits the particle, but the bonding force is higher than the force of the dresser, resulting in a grain that is being cut (broken). For the calculation of the dressing force F_t, an empirical formula was used [35]. It is based on the dressing depth a_{dp} (in mm) and the dresser travel speed f_d (in mm/min)

$$F_t = 9.631 \cdot {a_{dp}}^{-0.1992} \cdot {f_d}^{-0.1774} \tag{7}$$

The bonding force is dependent on material-specific properties for the bonding material [15]. In this study, a specific bonding force for the material of 800 N/mm^2 was used, depending on the surface area of each bonding a_j of a particle. Thus, the bonding force of a particle i is

$$F_{bi} = 800 \text{ N/mm}^2 \cdot \sum {}^{m}_{(j=1)} a_j. \tag{8}$$

5.1.4 Surface Calculation and Modelling

For the modelling of the grinding wheel topography, the software ParaView 5.7 was used. To properly display the surface, output points had to be defined in the MatLab simulation. Fig.11 displays how output points for different particles were created and how the surface was visualised using these points. In the first step, particles visible on the surface (top view) were identified. In the second step, the tip height of the particle was identified. In a third step, up to 16 additional data points were created to properly and realistically visualise the shape of the abrasive particles. Afterwards, these additionally created data points were checked for their spacing and eventually removed for smoothing the surface output and unintended spikes. In the last step the exported data points were connected and result in the topography.

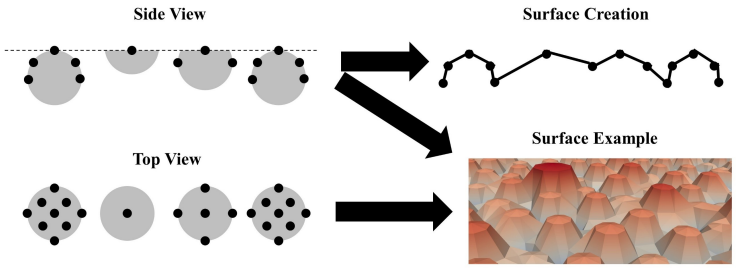

Figure 11 Visualization of the calculated surface.

All steps conducted during the simulation were visualised to enhance the understanding as well as checking for the reliability of the calculations and assumptions. Fig.12 shows an example of all the steps using the grit size 30 with a 5% compression.

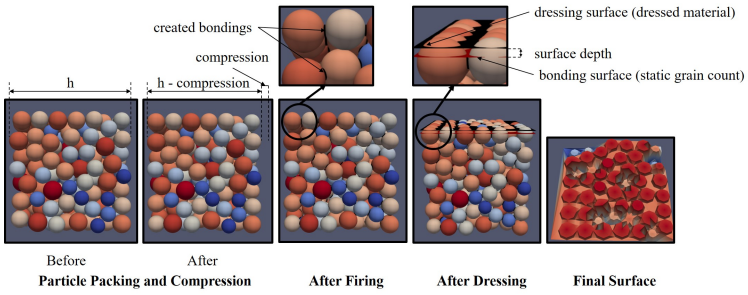

Figure 12 Visualization of the simulation steps.

5.2 Results and Discussion

The simulated grinding wheel topographies are assessed based on the output variables bonding strength and average grain count. The average bonding strength is the average of the bonding force of all the particles in the grinding wheel and their respective bondings. The static grain count is the number of grains on the wheel surface in a certain area [26].

In Fig.13 the average bonding strength is compared to different percentages of the compression strength for all grain sizes. The graph shows that an increasing particle size leads to higher average bonding strength. Thus, grit 24 had the highest maximum feasible average bonding strength with 149 N, and grit 60 the lowest, with 37 N. The characteristic slope of the bonding strength is very similar for different percentages of compression and is

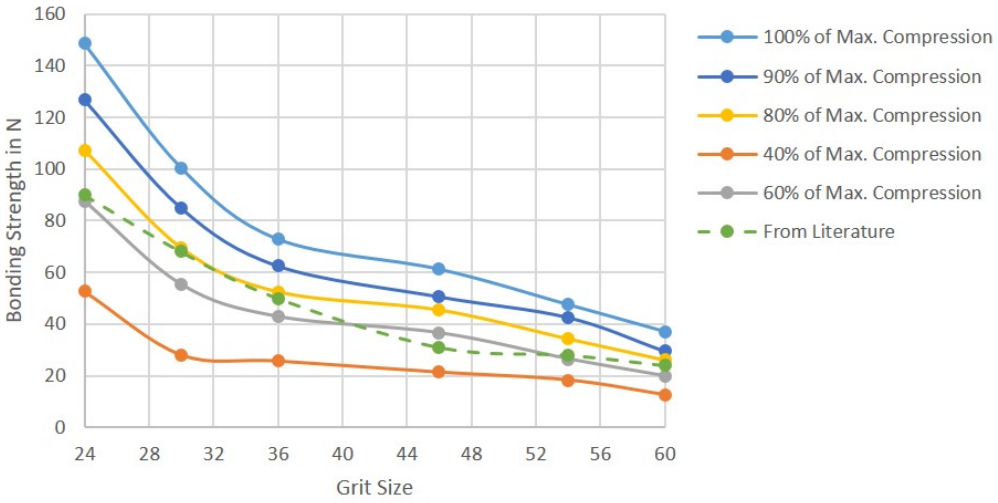

Figure 13 Average bonding strength depending on compression for different grit sizes and compared to values from [24].

very similar compared to empirical results [24]. The characteristic slope and maximum values fit well to the simulation of maximum compression, slightly varying along with different grit sizes.

The static grain count per cm^2, in comparison to the percentage of compression is displayed in Fig.14. For the maximum possible compression, the static grain count is the highest for grit 60, decreasing with grit size and having the lowest for grit 24, which is in line with empirical analysis [4], simulation [14] and theory [4]. Remarkably, all slopes for the different grit sizes show a similar characteristic. In the very beginning there is a slight, but constant increase, followed by an exponential increase, which turns into a constant value. Eventually, the slope remains constant for further compression. Thus, a value close to the maximum static grain count is reached before the maximum feasible compression.

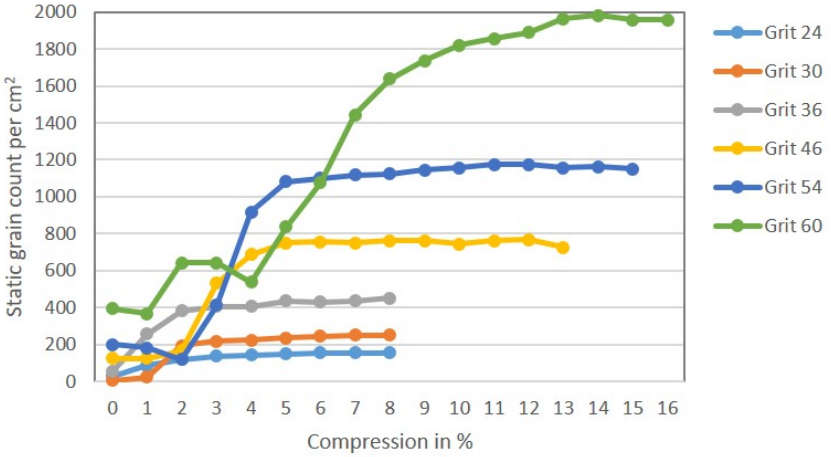

Figure 14 Static grain count dependent on different percentages of compression.

The surface calculated with Matlab was exported as a VTK file and processed using Paraview and its elevation grid filter, to provide a realistic surface of the exported data. The visualisation was enhanced by different colouring, according to height, bonding force, protrusion height and alternative protrusion height. The standard surface representation is coloured based on the lowest surface point in the respective area along with all compression percentages. It is visible that the surface is rather unstructured for low percentages of compression and a more even and structured surface is created with higher compression (see Fig.15). A very even and uniform surface is usually reached above 50 % of the maximum compression. It is also visible that with increasing compression, random surface caverns start disappearing, reducing the pore volume of the surface, as visible in Fig.15 Low percentages of compression might contain single grains that protrude from the surface which might leave unintended scratches while grinding. The surface topography appears to be similar to previous surface simulations with [14].

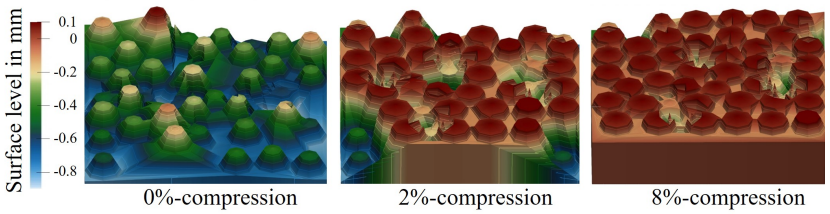

Figure 15 Exemplary surface topography of grit 30 for 0 %, 2% amd 8 % compression. Colormap indicates height above/below surface level in mm.

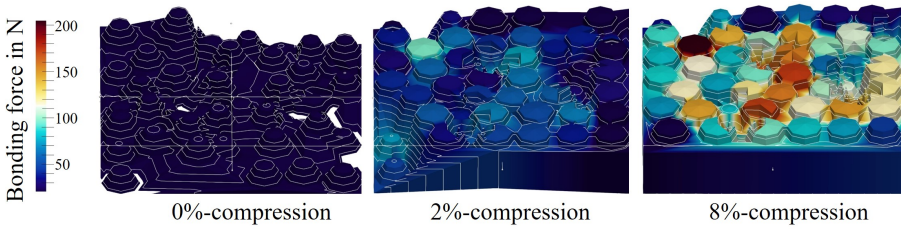

Figure 16 Bonding force of grit 30 for 0%, 2% and 8% compression. Colormap indicates the bonding forces in N.

To analyse the bonding strength of the grinding wheel, the surface was coloured to the respective bonding strength of a particle and the surrounding area, see Fig 16. For all grit sizes the characteristic development of the bonding force and the distribution is similar, just as the analysis of the bonding strength has shown. While the bonding force is very low at low compression, it increases with increasing compression. Although the distribution is evenly in the beginning, at higher compressions the differences in bonding force of the particles are visible. Though occasional particles stand out with a higher bonding force, but particles with low and higher bonding forces are equally distributed across the surface area.

6 Overview and Future work

To give a brief overview of the paper, four individual research studies were performed, and the most important findings are as follows:

- The first study was performed to parameterize the JC-model with respect to a micro indentation experiments. EBSD and CPFEM simulations were performed to understand

if the micro-structure of the workpiece material has an influence in material removal mechanism in a micro-indentation process. The fitting to the experimental data is only a little better for CPFEM model when compared to the JC-model. In the future studies, an extension to this comparative study will be done for a single grain scratch process, to understand the capabilities of both models to describe complex material removal mechanisms.

- In the second study, the influence of higher tool rake angles on the process forces in a micro-cutting process was analyzed with the help of a 2D orthogonal cutting model. Four different discretizational approaches (LAG, ALE, SPH and PFEM) were employed to model the workpiece A2024 T351 and to understand which approach is most suitable for metal cutting simulations. As a conclusion to this study, all the discretizational approaches were benchmarked with micro-cutting experiments found in literature [25]. The simulation models successfully predict the cutting forces with a maximum error of 8 % and the passive forces with an error of 40 %. From the sensitivity analysis performed with higher tool rake angles, the tendency is observed that the process forces increase with an increase in the negative tool rake angle from $\gamma = 20°$ to $\gamma = -45°$. This tendancy is also confirmed by the investigation performed in [12]. The model needs to be extended to a 3D simulation to also simulate material removal mechanisms such as plowing and rubbing, which is typically observed in a grinding/scratching process.
- In the third study, scratch experiments was performed to analyse the material removal process for a ductile material aluminium A2017 T4 and a brittle material soda lime glass. The experiments help to analyse the effect of change in the process forces (cutting forces, passive forces) under the influence of change in linear speed and changes in the depth of cuts a_p. Two conical indenter geometries ($\theta = 90°$ and $\theta = 120°$) were used to understand the effect of the change in the tool geometry. During the single grit scratching of glass, it is observed that the cutting forces reduce and the passive forces remains constant with increasing linear speeds. The cutting forces measured for the indenter geometries $\theta = 120°$ is higher in comparison to $\theta = 90°$, whereas the passive forces show an opposite tendancy. While performing the scratch experiments with aluminium, it was observed that the process forces reduce with the increase in the linear speed, which is also confirmed by literature [17].
- Finally for the fourth study, a realistic simulation of the manufacturing process of a grinding wheel was carried out, starting with the raw material, compression, sintering and dressing until the final grinding surface was developed. The bonding strengths and static grain count were analyzed and the tendencies were observed that an increasing percentage of compression was found to increase the bonding strength of particles. Furthermore, the larger the size of the abrasive particles, the higher is the bonding strength. The static grain count was found to increase with increasing compression and with decreasing particle size.

In conclusion, the first three research studies focuses on the microscopic scale of single grit-workpiece interactions. These studies help in the understanding of the single grain scratch process and thereby contributes to the final goal of developing a physical force model for single grit scratching. In future, these studies will be extended to enhance the capabilities of the physical force model for the single grit approach. The final study focuses on the macroscopic scale of grinding-workpiece interactions. The development of a virtual wheel topography is the first step that aids for upscalling the physical force model from the single grit scratch process to a complete grinding process.

References

1. P.J. Arrazola. *Modelisation numerique de la coupe: etude de sensibilite des parametres d'entree et identification du frottement entre outil-copeau.* PhD thesis, L'École Centrale de Nantes, 2003.
2. C.P. Bhateja and R.P. Lindsay. The importance of abrasive grinding wheel hardness control for the productivity of production grinding operations. *CIRP Annals*, 30(1):247–249, 1981.
3. B. Borsos, A. Csörgő, A. Hidas, B. Kotnyek, and G. Stépán. Two-Dimensional Finite Element Analysis of Turning Processes. *Periodica Polytechnica Mechanical Engineering*, 61(1):44–54, 2017.
4. X. Chen and W.B. Rowe. Analysis and simulation of the grinding process. part i: generation of the grinding wheel surface. *International Journal of Machine Tools and Manufacture*, 36(8):871–882, 1996.
5. D.A. Doman, R. Bauer, and A. Warkentin. Experimentally validated finite element model of the rubbing and ploughing phases in scratch tests. *Proceedings of the Institution of Mechanical Engineers, Part B: Journal of Engineering Manufacture*, 223(12):1519–1527, 2009.
6. A. Hillerborg, M. Modéer, and P. E. Petersson. Analysis of crack formation and crack growth in concrete by means of fracture mechanics and finite elements. *Cement and Concrete Research*, 6(6):773–781, 1976.
7. S. R. Idelsohn, E. Onate, and F. Del Pin. The particle finite element method: A powerful tool to solve incompressible flows with free-surfaces and breaking waves. *International Journal for Numerical Methods in Engineering*, 61(7):964–989, 2004.
8. M.J. Jackson. *A study of vitreous-bonded abrasive materials.* PhD thesis, Liverpool John Moores University, 1995.
9. G.R. Johnson and W.H. Cook. A constitutive model and data for metals subjected to large strains, high strain rates and high temperatures. In *Proceedings of the 7th International Symposium on Ballistics*, pages 541–547, 1983.
10. B. Kirsch, C. Effgen, M. Büchel, and J.C. Aurich. Comparison of the embodied energy of a grinding wheel and an end mill. *Procedia CIRP*, 15:74–79, 2014.
11. M.W Klein, B. Blinn, M. Smaga, and T. Beck. High cycle fatigue behavior of high-mn twip steel with different surface morphologies. *International Journal of Fatigue*, 134:105499, 2020.
12. S. Kosaraju, V. Anne, and V. Ghanta. Effect of Rake Angle and Feed Rate on Cutting Forces in an Orthogonal Turning Process. *International Conference on Trends in Mechanical and Industrial Engineering*, 61(May):150–154, 2011.
13. M. Li, W. Ding, B. Li, and J. Xu. Morphological evolution and grinding performance of vitrified bonded microcrystal alumina abrasive wheel dressed with a single-grit diamond. *Ceramics International*, 45(16):19669–19678, 2019.
14. X. Li. *Modeling and simulation of grinding processes based on a virtual wheel model and microscopic interaction analysis.* PhD thesis, Worcester Polytechnic Institute, 2010.
15. M. Hrairi M. Djemana. Modelling and Simulation of Impedance-Based Damaged Monitoring of Structures. *International Journal of Modelling and Simulation*, 15:395–408, 2016.
16. L. Olovsson, L. Nilsson, and K. Simonsson. ALE formulation for the solution of two-dimensional metal cutting problems. *Computers and Structures*, 72(4):497–507, 1999.
17. T. Opoz. *Investigation of Material Removal Mechanism in Grinding: A Single Grit Approach.* PhD thesis, University of Huddersfield, 2012.
18. D.T. Pierce, K. Nowag, A. Montagne, J.A. Jiménez, J.E. Wittig, and R. Ghisleni. Single crystal elastic constants of high-manganese transformation-and twinning-induced plasticity steels determined by a new method utilizing nanoindentation. *Materials Science and Engineering: A*, 578:134–139, 2013.
19. Manika Prasad, Malgorzata Kopycinska, Ute Rabe, and Walter Arnold. Measurement of young's modulus of clay minerals using atomic force acoustic microscopy. *Geophysical Research Letters*, 29(8):13–1–13–4, 2002.

20 J.M. Rodríguez, J.M. Carbonell, and P. Jonsén. Numerical Methods for the Modelling of Chip Formation. *Archives of Computational Methods in Engineering*, pages 1–48, 2018.

21 J.M. Rodríguez, J.M. Carbonell, J C. Cante, J. Oliver, and P. Jonsén. Generation of segmental chips in metal cutting modeled with the PFEM. *Computational Mechanics*, 61(6):639–655, 2018.

22 F. Roters, P. Eisenlohr, L. Hantcherli, D.D. Tjahjanto, T.R. Bieler, and D. Raabe. Overview of constitutive laws, kinematics, homogenization and multiscale methods in crystal plasticity finite-element modeling: Theory, experiments, applications. *Acta Materialia*, 58(4):1152–1211, 2010.

23 James F Shackelford. *Introduction to materials science for engineers*. Pearson Upper Saddle River, 2016.

24 M. C. Shaw. Principles of abrasive processing. In *Proceedings of the 32nd International MATADOR Conference*, 1996.

25 S. Subbiah. *Some investigations of scaling effects in micro-cutting*. PhD thesis, Georgia Institute of Technology, 2006.

26 S. Xu, D. Ruan, J.H. Beynon, and Y. Rong. Dynamic tensile behaviour of twip steel under intermediate strain rate loading. *Materials Science and Engineering: A*, 573:132–140, 2013.

27 Y.Y. Zhu, S.H. Liang, Z.J. Zhan, P. Xiao, and Z.K. Fan. Simulation of the change of sintering neck between two grains in two dimensions. *Acta Metallurgica Sinica (English Letters)*, 19(6):397–404, 2006.